ORIGINAL PAPER

Synthesis of porous C/Fe$_3$O$_4$ microspheres by spray pyrolysis with NaNO$_3$ additive for lithium-ion battery applications

Akylbek Adi[1] · Izumi Taniguchi[1]

Abstract

In this work, we successfully synthesized porous C/Fe$_3$O$_4$ microspheres by spray pyrolysis at 700°C with a sodium nitrate (NaNO$_3$) additive in the precursor solution. Furthermore, we studied their electrochemical properties as anode material for Li-ion batteries. The systematic studies by various characterization techniques show that NaNO$_3$ catalyzes the carbonization of sucrose and enhances the crystallization of Fe$_3$O$_4$. Moreover, an aqueous etching can easily remove sodium compounds to produce porous C/Fe$_3$O$_4$ microspheres with large surface areas and pore volumes. The porous C/Fe$_3$O$_4$ microspheres exhibit a reversible capacity of ~780 mAh g^{-1} in the initial cycles and ~520 mAh g^{-1} after 30 cycles at a current density of 50 mA g^{-1}. Moreover, a reversible capacity of ~400 mAh g^{-1} is attainable after 200 cycles, even at a high current density of 500 mA g^{-1}. The wide range of pores produced from the removal of sodium compounds might enable easy electrolyte penetration and facilitate fast Li-ion diffusion, while the N-doping can promote the electronic conductivity of the carbon. These features of porous C/Fe$_3$O$_4$ microspheres led to the improved electrochemical properties of this sample.

Keywords Spray pyrolysis · NaNO$_3$ additive · Porous C/Fe$_3$O$_4$ microspheres · Anode · Li-ion batteries

Introduction

The future of renewable energies and electric vehicles (EVs) are tightly correlated to further progress in Li-ion batteries [1]. Along with commercialized LiCoO$_2$ other cathode materials such as LiMn$_2$O$_4$ and LiFePO$_4$ have found their ways toward practical application [2–4]. In contrast, graphite remains mainly used as anode material due to its low working potential, cost-effectiveness, and good cycling stability [5]. However, this anode cannot meet the high power/energy density requirements for renewable energies and EVs owing to its low theoretical capacity (372 mAh g^{-1}) [6]. Therefore, advanced anode materials with superior electrochemical properties are urgently demanded to be designed and synthesized.

Among various possible materials, iron oxide (Fe$_3$O$_4$) is considered to be a promising anode material for next-generation Li-ion batteries due to its high theoretical capacity (924 mAh g^{-1}), abundance in the Earth's crust, and environmental friendliness [7, 8]. However, bulk Fe$_3$O$_4$ particles suffer from rapid capacity fading owing to their low electrical conductivity and colossal volume change during lithiation/delithiation processes [9, 10]. Two main approaches have been successfully applied to overcome these issues, such as a synthesis of nanostructured Fe$_3$O$_4$ particles and its integration with carbon materials [11–15]. However, Li-ion battery application requires these composite materials to possess an appropriate morphology that ensures a high contact area between Fe$_3$O$_4$ nanoparticles and electrolytes; and to be prepared by simple and cost-effective methods.

Thus far, Fe$_3$O$_4$ dispersed/decorated carbon materials have been prepared mainly by hydrothermal/solvothermal [16, 17], co-precipitation [18, 19], and electrospinning [20, 21] methods. Although these composite materials demonstrated an improved electrochemical performance when applied as anode materials for Li-ion batteries, the preparation of these materials rely on the complicated and time-consuming procedures, and require expensive toxic reagents. Compared with these methods, spray pyrolysis (SP) can provide a simple, short processing, and continuous synthesis route for multifunctional materials with homogeneous chemical composition and diverse structures [22–24]. Moreover, an easy variation of a starting solution can offer numerous opportunities to synthesize various multicomponent composite materials with excellent chemical and

✉ Izumi Taniguchi
taniguchi.i.aa@m.titech.ac.jp; itaniguc@chemeng.titech.ac.jp

1 Department of Chemical Science and Engineering, Tokyo Institute of Technology, Tokyo 152-8552, Japan

physical flexibility. Despite many advantages of SP, there have been very few reports on a direct synthesis of C/Fe$_3$O$_4$ composite materials by SP [25–27]. For example, Choi et al. reported a macroporous Fe$_3$O$_4$/carbon composite synthesis by SP with polymer additives as anode materials for Li-ion batteries [26]. As a cost-effective alternative for the polymer additives, Atkinson et al. [27] used inorganic salt additives such as sodium chloride (NaCl) and sodium nitrate (NaNO$_3$) to produce iron-impregnated porous carbon (Fe–C) spheres for catalytic application. However, to the best of our knowledge, the effect of NaNO$_3$ additive on a phase conversion of Fe$_3$O$_4$ nanoparticles, morphology evolution of C/Fe$_3$O$_4$ microspheres, and their potential application in lithium-ion batteries have not been reported.

Recently, we reported a synthesis of porous-crystalline C/Fe$_3$O$_4$ microspheres by spray pyrolysis with post oxidation under steam atmosphere [28]. Here we chemically activated C/Fe$_3$O$_4$ microspheres with a sodium nitrate (NaNO$_3$) additive in the precursor solution to ensure a high contact area between Fe$_3$O$_4$ nanoparticles and electrolyte. This approach provides a facile and cost-effective way to prepare porous C/Fe$_3$O$_4$ microspheres. We investigated the effect of NaNO$_3$ additive on a phase conversion of Fe$_3$O$_4$ nanoparticles, morphology evolution of C/Fe$_3$O$_4$ microspheres, and their electrochemical performances as an anode material for Li-ion batteries in detail by various physical and electrochemical characterization techniques.

Experimental section

Synthesis of porous C/Fe$_3$O$_4$ microspheres

All analytically pure chemicals were purchased from FUJI-FILM Wako Pure Chem. Corp., Japan, and used as-is. The precursor solutions were prepared by dissolving 0.50 M sucrose and 0.015 M iron (III) nitrate nonahydrate (FeNO$_3$)$_3$·9H$_2$O) in distilled water at room temperature. Sodium nitrate (NaNO$_3$) was then added to the solution at different concentrations ranging from 0 to 2.00 M. The solutions were magnetically stirred to dissolve the reagents completely.

A schematic diagram of the spray pyrolysis setup has been described elsewhere [24]. It consists of an ultrasonic nebulizer (1.7 MHz, Omron Co., Ltd., Model NE–U17), a laminar flow aerosol reactor (a high-quality ceramic tube with an inner diameter of 20 mm and a length of 150 cm), and an electrostatic precipitator. The nebulizer continuously atomized the starting solution at a frequency of 1.7 MHz. The generated droplets were carried into the pre-heated reactor tube (700ºC) by high-purity nitrogen gas (1.0 L min^{-1}). The electrostatic precipitator collected the particles at 180ºC to prevent vapor condensation on the particles, while a cold trap was set to condense evolved gases. The samples prepared with NaNO$_3$ additive were washed several times with a distilled water and ethanol mixture to remove the remaining sodium salts (Fig. S1a) and dried at 110ºC for 6 h in a vacuum oven.

Physical characterization

The crystal phase of C/Fe$_3$O$_4$ microspheres was identified using an X-ray (Rigaku, Ultima IV with D/teX Ultra) diffractometer with monochromated Cu Kα radiation. The morphology of the samples was observed by SEM (KEYENCE, VE-9800SP). The measurements and the calculation of the particle size distribution, geometric mean diameter $d_{p,g}$, and geometric standard deviation σ_g have been described elsewhere [29]. The microstructure and elemental distributions of the samples were characterized by field-emission TEM (FE-TEM, JEOL Ltd., JEM2010F) at 200 kV with EDS (Genesis).

The composition of the samples was quantified by a CHNS elemental analyzer (Elementar, Vario Micro Cube), and thermogravimetry and differential thermal analysis (TG-DTA, Rigaku TG8120). The carbon structure was analyzed by Raman spectroscopy (NRS–2100, JASCO Co.). The XPS (JEOL Ltd., JPS-9010) was performed to clarify the chemical nature and valence state of the elements on the surface of samples.

The nitrogen adsorption-desorption isotherms were obtained using a Micrometrics Tristar II 3020 system to calculate the specific surface area and pore volumes of the samples. The specific surface area was calculated by the Bruneaur–Emment–Teller (BET) method. Total pore volume and micropore volume were evaluated using the Gurvich rule and t-plot method, respectively.

Electrochemical characterization

The electrochemical properties of C/Fe$_3$O$_4$ microspheres were evaluated in CR2032 coin-type cells with lithium metal as reference and counter electrodes. To prepare the working electrodes, 75 wt.% active materials, 15 wt.% acetylene black (AB), and 10 wt.% polyvinylidene fluoride (PVDF) were mixed in N-methyl-2-pyrrolidone (NMP) to obtain the slurry. The slurry was then coated onto a Cu foil current collector by doctor blade technique. The coated electrodes were dried at 110ºC for 5 h in a vacuum oven, roll-pressed to enhance the contact between the electrode material and the current collector, and punched into round disks of 15.9 mm in diameter. The area of the electrode material was then standardized into 1×1 cm^2 by scratching. The mass loading of the active materials was about 1.0 ± 0.1 mg cm^{-2}. The CR2032 coin-type cells were assembled in a high-purity-argon-filled glove box. A commercially available electrolyte of 1.0 mol L^{-1} lithium hexafluorophosphate (LiPF$_6$) dissolved in a mixture of ethylene carbonate (EC) and dimethyl carbonate (DMC) was used. The separators were kept in the electrolyte for a couple of weeks before use to let the separator

thoroughly soak the electrolyte. The assembled cells were galvanostatically cycled in the potential window of 0.01–3.00 V (vs. Li/Li$^+$) at a current density of 50 mA g^{-1} using multichannel battery testers (Hokuto Denko, HJ101mSM8A). The rate performance tests were conducted at different current densities from 50 to 2000 mA g^{-1}. The electrode material's current density and specific capacity were calculated based on the mass of active materials. Cyclic voltammetry (CV) analysis was performed in the potential window of 0–3.00 V (vs. Li/Li+) at a scan rate of 0.1 mV s^{-1}. Electrochemical impedance spectroscopy (EIS) measurements were conducted in the range of 100 kHz to 0.1 Hz using a Solartron 1255B frequency response analyzer connected to a Solartron SI 1287 electrochemical interface. All electrochemical measurements were performed at room temperature.

Results and discussion

Synthesis and physical characterization of porous C/Fe$_3$O$_4$ microspheres

Figure 1 shows the XRD patterns of C/Fe$_3$O$_4$ microparticles prepared by SP with different concentrations of NaNO$_3$ additive. The sample prepared without additive had XRD peaks corresponding to amorphous carbon and Fe$_3$O$_4$ without impurity [30–32]. The sucrose decomposition products
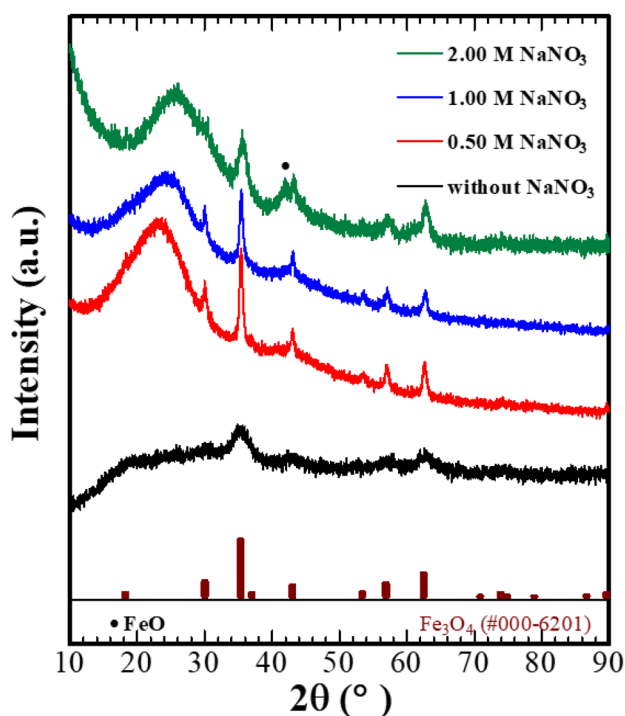

Fig. 1 XRD patterns of C/Fe$_3$O$_4$ microspheres prepared by SP with different concentrations of NaNO$_3$ additive

partially reduced Fe^{3+} ions into Fe^{2+} ions during the synthesis, producing Fe$_3$O$_4$ instead of Fe$_2$O$_3$ from the single Fe^{3+} precursor solution [33]. The peaks of Fe$_3$O$_4$ and carbon remained in the XRD patterns of the samples prepared with 0.50 and 1.00 M NaNO$_3$ additive after the aqueous removal of sodium salts. However, the sample prepared with 2.00 M NaNO$_3$ additive had an additional peak of the impurity phase. The XRD peaks of carbon and Fe$_3$O$_4$ intensified in the samples prepared with NaNO$_3$ additive due to the enhanced carbonization of sucrose and crystallization of Fe$_3$O$_4$, respectively.

Figure 2 shows the SEM images of C/Fe$_3$O$_4$ microparticles prepared by SP with different concentrations of NaNO$_3$ additive. The composite prepared without additive had a spherical morphology with a smooth surface (Fig. 2a). On the other hand, the presence of NaNO$_3$ additive in the precursor solution significantly affected the morphology of the final microparticles. For example, the synthesis with 0.50 M NaNO$_3$ additive produced sheet-like microparticles and spherical microparticles (Fig. 2b), but an increase in the additive concentration to 1.00 M formed mainly spherical microparticles (Fig. 2c). Such morphology evolution was attributed to a supersaturation degree of aerosol droplets, determining whether the precipitation occurs on the surface or throughout the entire droplet [34, 35]. A further increase in the concentration of NaNO$_3$ (2.00 M) led to the collapse of microstructure (Fig. 2d). Moreover, the presence of NaNO$_3$ in the precursor solution enlarged the geometric mean diameter of C/Fe$_3$O$_4$ microspheres from 0.47 to 1.11 μm (Fig. S2) owing to the increase in the amount of carbonized sucrose (Table 1). The content of carbon and Fe$_3$O$_4$ in the composites prepared with 1.00 M NaNO$_3$ was further confirmed by TG/DTA analysis, as shown in Fig. S3. The prepared microspheres had ~20 wt.% of Fe$_3$O$_4$ calculated based on the weight of Fe$_2$O$_3$ as the final oxidation product. As this content of Fe$_3$O$_4$ is relatively low compared with other reported composites, the spray pyrolysis synthesis was performed with a higher concentration of iron source (0.06 M) in the precursor solution to increase the content of Fe$_3$O$_4$. However, the impurity peaks of FeO appeared in the XRD pattern of this sample (Fig. S4). Therefore, it is not easy to simultaneously increase the content of Fe$_3$O$_4$ and ensure its purity.

Figure 2e and f show the TEM images of C/Fe$_3$O$_4$ microspheres prepared by SP without and with 1.00 M NaNO$_3$ additive, respectively. The sample prepared without additive had ultrafine-sized Fe$_3$O$_4$ nanoparticles densely dispersed in the carbon matrix (Fig. 2e). The sucrose and its decomposition products sterically hindered the aggregation and growth of iron oxide nucleus [33]. On the other hand, the TEM images of the sample prepared with 1.00 M NaNO$_3$ additive showed larger Fe$_3$O$_4$ nanoparticles (20–30 nm in diameter) evenly dispersed mainly on the surface of the carbon microsphere (Fig. 2f). The molten NaNO$_3$ may increase the
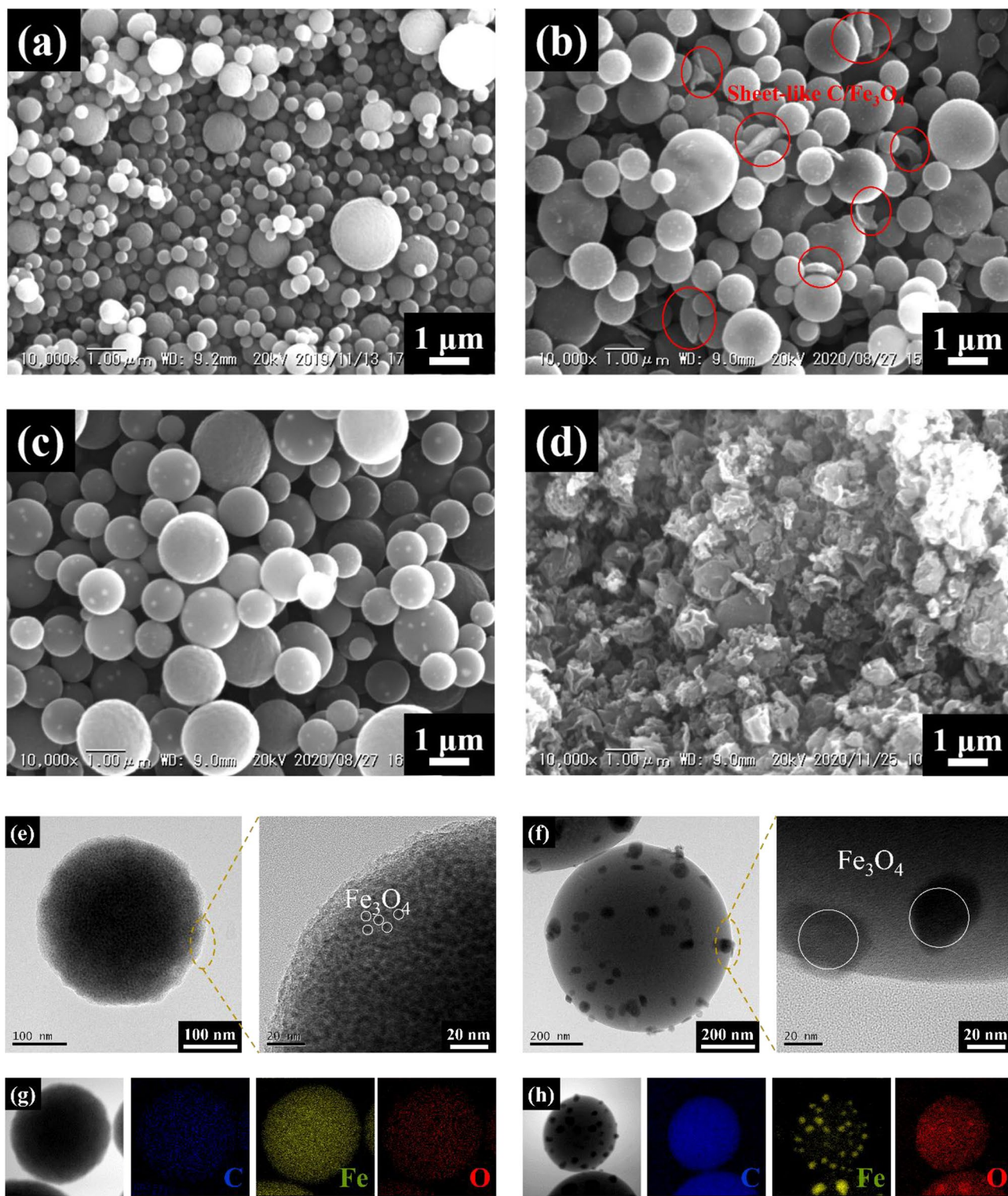
Fig. 2 SEM images of C/Fe$_3$O$_4$ microspheres prepared by SP without (**a**) and with 0.50 M (**b**), 1.00 M (**c**), and 2.00 M (**d**) NaNO$_3$ additive; TEM and TEM-EDX images of C/Fe$_3$O$_4$ microspheres prepared without (**e**, **g**) and with (**f**, **h**) 1.00 M NaNO$_3$ additive

surface energy of Fe$_3$O$_4$ nanoparticles, thus leading to their diffusion and crystal growth. The corresponding elemental mapping shows the presence of carbon (C), iron (Fe), and oxygen (O) elements in both samples, further verifying the formation of carbon microspheres with evenly dispersed Fe$_3$O$_4$ nanoparticles (Fig. 2g, h).

Table 1 CHNS results of C/Fe$_3$O$_4$ microspheres prepared SP with different concentrations of NaNO$_3$ additive

NaNO$_3$ concentration	C (wt.%)	H (wt.%)	N (wt.%)	S (wt.%)
without	41	1	0	0
0.50 M	65	3	2	1
1.00 M	60	3	4	0
2.00 M	54	2	6	0

Figure 3a shows the nitrogen adsorption-desorption isotherms of C/Fe$_3$O$_4$ microspheres prepared by SP with different concentrations of NaNO$_3$ additive. The microspheres prepared with 0.50 and 1.00 M NaNO$_3$ additive had an increased nitrogen uptake at a low relative pressure region (P/P$_0$ = 0.01), which originates from the micropore filling. In addition, the former sample shows a combination of type I and II or III isotherms, suggesting the presence of micro-, meso-, and macropores. On the other hand, the sample prepared with 1.00 M NaNO$_3$ additive had a hysteresis loop at a high relative pressure region (P/P$_0$ = 0.5–1.0), corresponding to type IV isotherms with H3 hysteresis [36]. Such isotherms originate from the capillary condensation in the mesopores and suggest the presence of mainly mesopores along with micropores in this sample. However, a further

increase in the concentration of NaNO$_3$ (2.00 M) led to the collapse of microstructure. The BET-surface area and pore volumes of C/Fe$_3$O$_4$ microspheres are summarized in Table 2. The use of NaNO$_3$ additive produced porous C/Fe$_3$O$_4$ microparticles with higher specific surface areas and pore volumes. Accordingly, the sample prepared with 1.00 M NaNO$_3$ additive had the largest specific surface area of 704 m^2 g^{-1} and total pore volume of 1.00 cm^3 g^{-1}.

Figure 3b shows the Raman spectra of C/Fe$_3$O$_4$ microspheres prepared with and without 1.00 M NaNO$_3$ additive. The spectra of both samples had two typical peaks at ~1358 and ~1591 cm^{-1}, corresponding to D and G bands of carbon, respectively. The D band was Raman active A$_{1g}$ mode associated with the vibration on sp^3–bonded disordered carbon atoms. The G band was Raman active E$_{2g}$ mode associated with the vibration on all sp^2–bonded ordered carbon atoms in a graphene layer [37, 38]. The peak intensity ratio of these peaks (I_D/I_G) reflects a graphitization degree of carbon in the microspheres. The ratio of I_D/I_G was lower in the sample prepared without the NaNO$_3$ additive (I_D/I_G=0.78) than the one prepared with the additive (I_D/I_G=0.95), indicating that the carbon had a lower degree of graphitization in the sample prepared with NaNO$_3$ additive. According to the above results, the spray pyrolysis without NaNO$_3$ additive produced a more uniform and dense carbon. On the other hand,

Fig. 3 N$_2$ sorption isotherms (**a**), Raman spectra (**b**), wide-scan XPS spectra (**c**), and N 1s XPS spectra of C/Fe$_3$O$_4$ microspheres prepared by SP with different concentrations of NaNO$_3$ additive
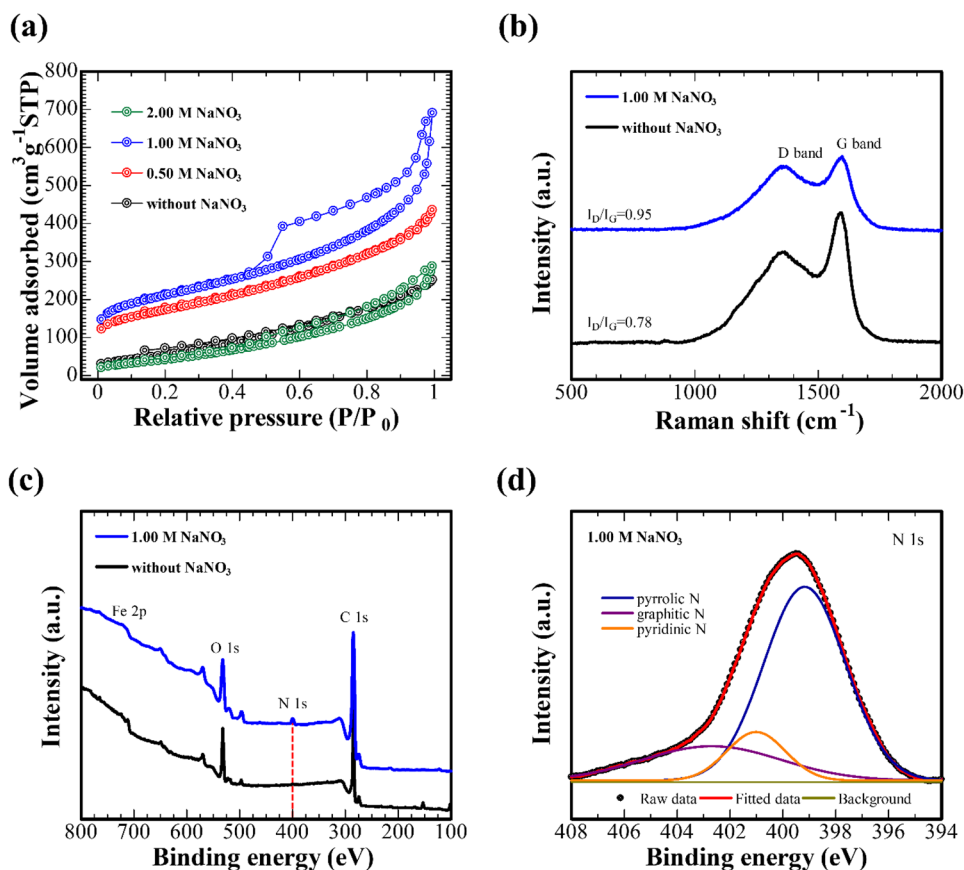
Table 2 BET surface area and pore volume of C/Fe$_3$O$_4$ microspheres prepared by SP with different concentrations of NaNO$_3$ additive

NaNO$_3$ concentration	BET surface area (m^2 g^{-1})	Micropore volume by t-plot (cm^3 g^{-1})	Meso- to Macro-pore volume (cm^3 g^{-1})	Total pore volume by Gurvich rule (cm^3 g^{-1})
without	201	≅0	0.34	0.34
0.50 M	580	0.08	0.56	0.66
1.00 M	704	0.11	0.89	1.00
2.00 M	170	≅0	0.43	0.43

the synthesis with NaNO$_3$ additive produced wide-range of pores, which might be responsible for the lower degree of graphitization in this sample [39].

Figure 3c shows the wide-scan XPS spectra of C/Fe$_3$O$_4$ microspheres prepared with and without 1.00 M NaNO$_3$ additive. The spectra further confirmed the presence of C 1s, N 1s, O 1s, and Fe 2p in the prepared samples. The N 1s indicated a formation of N-doped carbon, which was consistent with CHNS results (Table 1). This spectrum was deconvoluted into three typical bonds of nitrogen: graphitic, pyrrolic, and pyridinic (Fig. 3d). These nitrogen bonds can induce the electronic structure of carbon and promote its electronic conductivity [40].

The formation mechanism of porous C/Fe$_3$O$_4$ microspheres prepared by SP with NaNO$_3$ additive is graphically shown in Fig. 4. In the case of the SP synthesis without NaNO$_3$ additive (Fig. 4a), the ultrasonic nebulizer first

generates aerosol droplets that contain Fe^{3+} ions and partially hydrolyzed sucrose molecules. Hydrolysis of sucrose produces glucose and fructose molecules in an acidic solution (1) [33]. When the droplet enters the reactor, it starts to evaporate, creating a solid residue. The residue may contain sucrose, glucose, fructose, and Fe(OH)$_3$ or FeOOH. The formation of iron hydroxides might be due to the hydrolysis of Fe^{3+} ions at higher temperatures (2), which glucose will then reduce to form Fe$_3$O$_4$, gluconic acid, and hydrogen. When the sucrose melts, it produces even more glucose molecules [41], which evenly adsorb on Fe(OH)$_3$ or FeOOH, preventing their aggregation similar to conventional surfactant agents. Finally, the decomposition and carbonization of Fe(OH)$_3$ or FeOOH/glucose can produce the C/Fe$_3$O$_4$ microspheres. Note that there is no carbon isolation from sucrose-only precursor solution in this synthesis. Another possible mechanism for the formation of Fe$_3$O$_4$ might be

(a) Synthesis of dense C/Fe$_3$O$_4$ microspheres (without NaNO$_3$ additive)

1. Evaporation of solvent
2. Precipitation of solute
3. Melting of sucrose (160~190°C)
4. Decomposition and carbonization
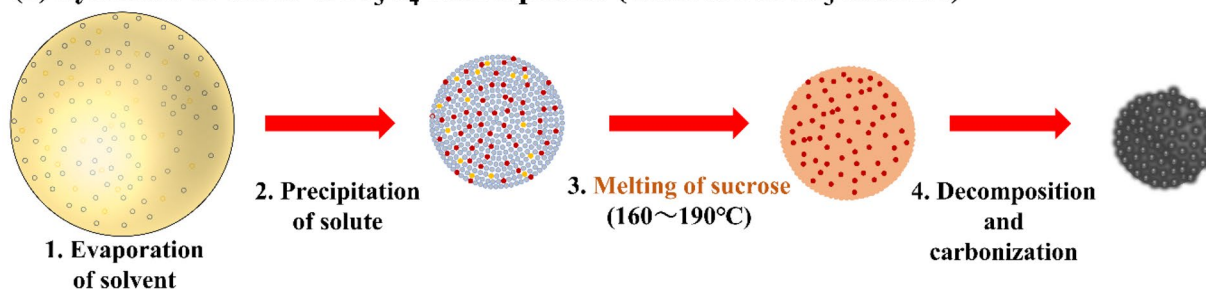
(b) Synthesis of porous C/Fe$_3$O$_4$ microspheres (with 1.00 M NaNO$_3$ additive)

1. Evaporation of solvent
2. Precipitation of solute
3. Melting of sucrose (160~190°C)
4. Melting and decomposition of NaNO$_3$ (308°C)
5. Decomposition and carbonization

○ Sucrose   ● Fe(NO$_3$)$_3$ ● Fe(OH)$_3$ or α-FeOOH   ● NaNO$_3$ ● Fe$_3$O$_4$ ○ Na$_2$CO$_3$
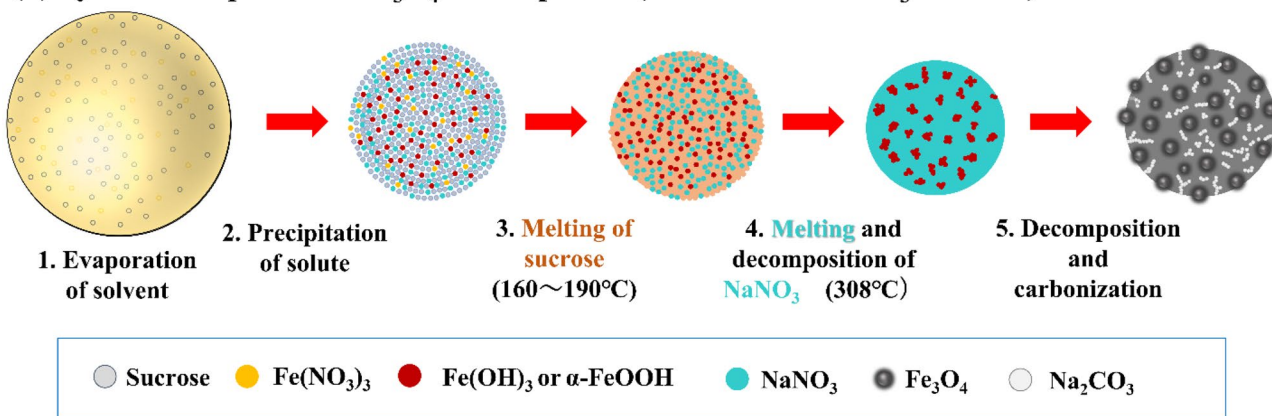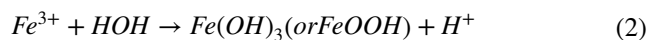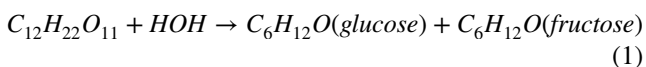
Fig. 4 Formation mechanism of porous C/Fe$_3$O$_4$ microspheres prepared by SP with NaNO$_3$ additive

the reduction of Fe_2O_3 (a direct decomposition product of $Fe(NO)_3$) by the decomposition products of sucrose.

$$C_{12}H_{22}O_{11} + HOH \rightarrow C_6H_{12}O(glucose) + C_6H_{12}O(fructose) \tag{1}$$

$$Fe^{3+} + HOH \rightarrow Fe(OH)_3(orFeOOH) + H^+ \tag{2}$$

In contrast, the SP synthesis of porous C/Fe_3O_4 microspheres with $NaNO_3$ additive proceeds with some additional
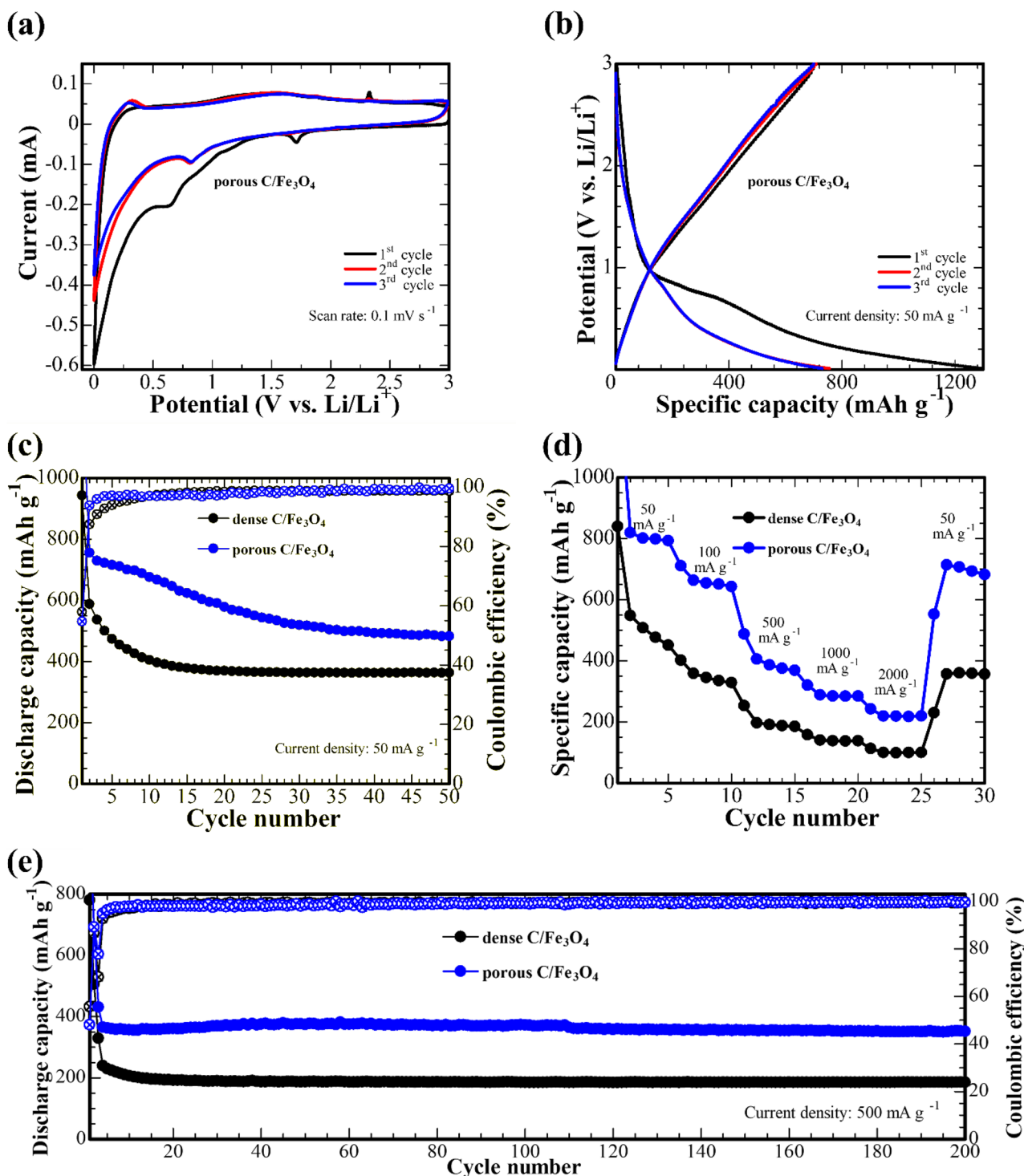

Fig. 5 CV curves (**a**) at a scan rate of 0.1 mV s^{-1}, charge-discharge curves (**b**) at a current density of 50 mA g^{-1}, cycling performance (**c**) at a current density of 50 mA g^{-1}, C-rate performances (**d**), and long-term cycling performances (**e**) at a current density of 500 mA g^{-1} of C/Fe_3O_4 microspheres prepared by SP with and without 1.00 M $NaNO_3$ additive

steps: the melting and decomposition of $NaNO_3$ (Fig. 4b-4). The molten $NaNO_3$ may increase the surface energy of Fe_3O_4 nanoparticles, leading to their agglomeration and crystallization (Fig. 4b-4). Furthermore, the decomposition products of $NaNO_3$ react with CO_x gases generated from the decomposition of sucrose to produce sodium compounds such as Na_2CO_3 (Fig. S1a). Aqueous etching can easily remove these sodium compounds to produce porous C/Fe_3O_4 microspheres with large surface areas and pore volumes. Moreover, $NaNO_3$ additive catalyzes the carbonization of sucrose, leading to an increase in carbon content and particle size.

From the above results, it can be concluded that the SP with a 1.00 M $NaNO_3$ additive can successfully produce porous C/Fe_3O_4 microspheres with large surface areas and pore volumes. Moreover, the systematic studies by various characterization techniques showed that $NaNO_3$ additive catalyzes the carbonization of sucrose and enhances the crystallization of Fe_3O_4.

Electrochemical characterization of porous C/Fe₃O₄ microspheres as an anode material for Li-ion batteries

Figure 5a shows the CV curves of porous C/Fe_3O_4 microspheres prepared by SP with 1.00 M $NaNO_3$ additive in the potential window of 0–3.00 V (vs. Li/Li$^+$) at a scan rate of 0.1 mV s^{-1}. The first cathodic scan revealed weak (at ~1.68 V) and strong (at ~0.50 V) peaks, respectively, corresponding to Li-ion insertion into Fe_3O_4 lattice ($Fe_3O_4 + xLi^+ + x\bar{e} \leftrightarrow Li_xFe_3O_4$ ($0 \leq x \leq 2$)) and its subsequent reduction to Fe^0 ($Li_xFe_3O_4 + (8–x)Li^+ + (8–x)\bar{e} \leftrightarrow 3Fe^0 + 4Li_2O$), as well as a formation of solid electrolyte interface (SEI) layer [42, 43]. Moreover, a sharp cathodic peak near 0 V could be attributed to a reversible lithiation of carbon ($2C + Li^+ + \bar{e} \leftrightarrow LiC_2$) [44]. On the other hand, the anodic scan revealed a broad peak ranging from ~1.1 to 1.8 V assigned to the delithiation of carbon and reversible oxidation of Fe^0 to Fe^{2+} and Fe^{3+} [45]. The anodic scan also revealed a peak at ~2.3 in the CV curves of this sample. Similar peaks appeared in the CV curves of sandwich-structured carbon nanotube/Cu_xO_y/Cu composite, which was assigned to the electrochemically active copper oxide in the interface between the Cu foil and carbon nanotube [46]. Mao et al. [47] also attributed such high potential peaks to the partially oxidized Cu formed during the drying of electrode coated Cu foil in air atmosphere. Therefore, the appearance of this peak in the CV curves of porous C/Fe_3O_4 microspheres might be due to these partially oxidized Cu foil or some irreversible side reactions as it disappeared in the third cycle.

Figure 5b shows the first three charge/discharge curves of porous C/Fe_3O_4 microspheres prepared by SP with 1.00 M $NaNO_3$ additive in the potential window of 0.01–3.00 V (vs.

Li/Li$^+$) at a current density of 50 mA g^{-1}. A sizeable irreversible capacity loss in the first cycle was attributed to the formation of SEI layer and structural modification of the electrode. Nevertheless, the specific capacity was stabilized from the second cycle with a high charge/discharge capacity of ~780 mAh g^{-1}, confirming reversible electrochemical performance. Figure 5c shows the corresponding cycling performances of dense and porous C/Fe_3O_4 microspheres prepared by SP with and without 1.00 M $NaNO_3$ additive in the potential window of 0.01–3.00 V (vs. Li/Li$^+$) at a current density of 50 mA g^{-1}. The porous C/Fe_3O_4 microspheres delivered a higher specific capacity of ~780 mAh g^{-1} in the initial cycles and ~520 mAh g^{-1} after 30 cycles than the dense microspheres. The cycle performance of porous C/Fe_3O_4 microspheres at a current density of 100 mA g^{-1} was also shown in Fig. S5. The enhanced electrochemical performances of C/Fe_3O_4 microspheres were attributed to the porous morphology with large surface areas and pore volumes.

Figure 5d shows the rate performance of dense and porous C/Fe_3O_4 microspheres prepared by SP with and without 1.00 M $NaNO_3$ additive in the potential window of 0.01–3.00 V (vs. Li/Li$^+$) at a series of current densities. The porous C/Fe_3O_4 microspheres had a better rate performance than the dense C/Fe_3O_4 microspheres at all current densities. Moreover, the specific capacity of porous C/Fe_3O_4 microspheres could recover to ~700 mAh g^{-1} when the current returns to a lower rate, indicating their good reversibility. The wide range of pores produced from the removal of sodium compounds might enable easy electrolyte penetration and
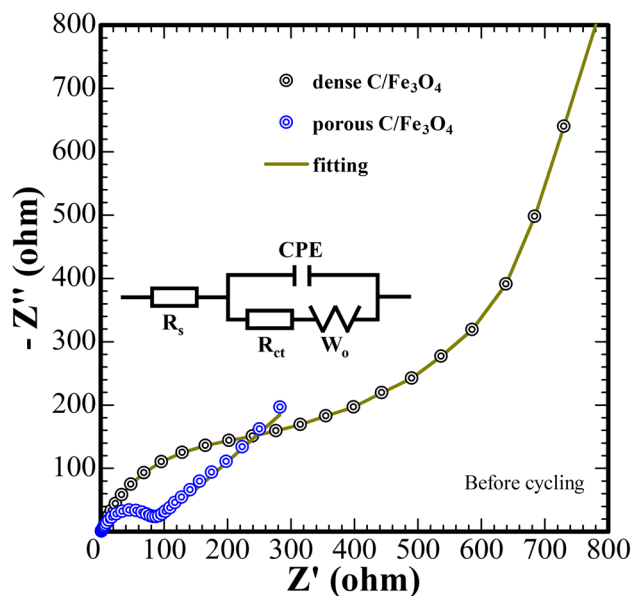

Fig. 6 Electrochemical impedance spectra of C/Fe_3O_4 microspheres prepared by SP with and without 1.00 M $NaNO_3$ additive before cycling and Randles equivalent circuit (the inset)
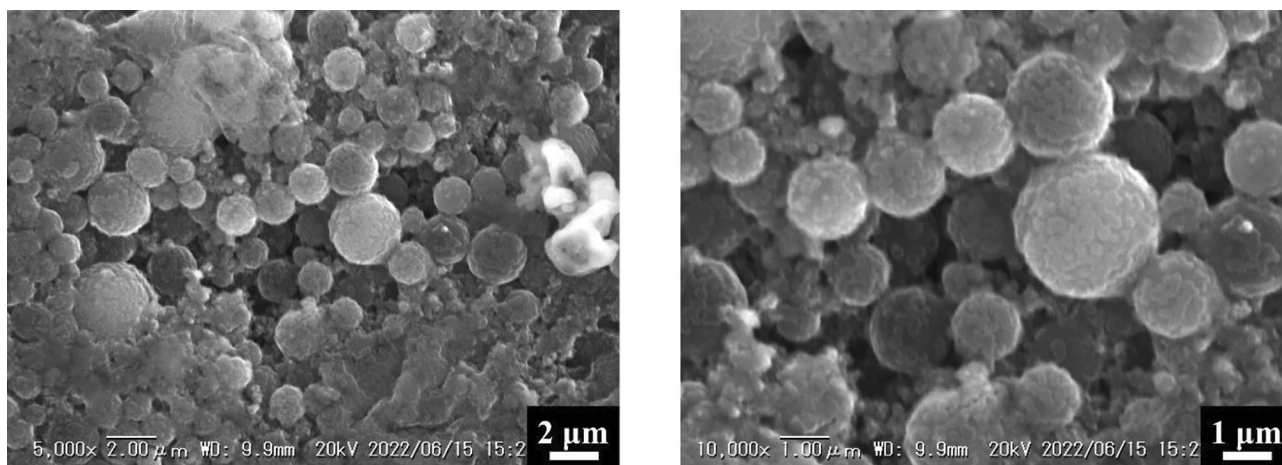
Fig. 7 SEM images of the porous C/Fe$_3$O$_4$ microspheres after 200 charge/discharge cycles at a current density of 500 mA g^{-1}

facilitate fast Li-ion diffusion, while the N-doping can promote the electronic conductivity of the carbon. These features of porous C/Fe$_3$O$_4$ microspheres led to the improved rate capability of this sample.

Figure 5e shows the long-term cycling performances of dense and porous C/Fe$_3$O$_4$ microspheres prepared by SP with and without 1.00 M NaNO$_3$ additive in the potential window of 0.01–3.00 V (vs. Li/Li$^+$) at a current density of 500 mA g^{-1}. Both samples demonstrated a stable cycling performance thanks to the carbon matrix's suppressed volume expansion of Fe$_3$O$_4$ nanoparticles. However, the porous C/Fe$_3$O$_4$ microspheres had a two-fold higher specific capacity of ~400 mAh g^{-1} than the dense microspheres (~200 mAh g^{-1}) at all over cycles. The appropriate morphology of porous C/Fe$_3$O$_4$ microspheres ensures a high contact area between Fe$_3$O$_4$ nanoparticles and electrolyte, leading to a better utilization of Fe$_3$O$_4$ nanoparticles. Moreover, the CV measurements of this sample showed that the N-doped carbon can reversibly react with Li-ions in the specified potential window. Considering the composition of the composite material, it can be seen that the N-doped carbon has a substantial contribution to the specific capacity of the composite.

Figure 6 shows the electrochemical impedance spectra of dense and porous C/Fe$_3$O$_4$ microspheres prepared by SP with and without 1.00 M NaNO$_3$ additive before cycling. The spectra of both samples had a semicircle in the high to medium frequency range and an inclined line in the low-frequency region associated with the charge transfer resistance and Warburg resistance, respectively. A lower charge transfer resistance accelerates the reaction kinetics of the electrodes. The porous C/Fe$_3$O$_4$ microspheres had much smaller charge transfer resistance than their dense counterparts. Accordingly, this sample demonstrated a higher specific capacity and enhanced rate performances.

The morphology stability of porous C/Fe$_3$O$_4$ microspheres for repeated lithiation/delithiation processes was observed by SEM, as shown in Figure 7. The electrode material preserved its initial spherical morphology even after 200 cycles at a current density of 500 mA g^{-1}. The appropriate morphology of porous C/Fe$_3$O$_4$ microspheres with a wide range of pores can effectively withstand substantial volume expansion of Fe$_3$O$_4$ nanoparticles, leading to the stable cycling stability of the sample.

Conclusion

In conclusion, we prepared porous C/Fe$_3$O$_4$ microspheres by simple and cost-effective spray pyrolysis with NaNO$_3$ additive and studied their electrochemical properties as anode material for Li-ion batteries. The systematic characterizations were performed to investigate the effects of NaNO$_3$ on the physical and electrochemical properties of the samples. The XRD, SEM, TEM, and CHNS results showed that NaNO$_3$ catalyzes the carbonization of sucrose and enhances the crystallization of Fe$_3$O$_4$. Moreover, nitrogen adsorption/desorption analysis showed that the aqueous removal of sodium compounds produces porous C/Fe$_3$O$_4$ microspheres with large surface areas and pore volumes. The porous C/Fe$_3$O$_4$ microspheres exhibited a reversible capacity of ~780 mAh g^{-1} in the initial cycles and ~520 mAh g^{-1} after 30 cycles at a current density of 50 mA g^{-1}. Moreover, a reversible capacity of ~400 mAh g^{-1} was attainable after 200 cycles, even at a high current density of 500 mA g^{-1}. The wide range of pores produced from the removal of sodium compounds might enable easy electrolyte penetration and facilitate fast Li-ion diffusion, while the N-doping can promote the electronic conductivity of carbon. These features of porous C/Fe$_3$O$_4$ microspheres led to the improved electrochemical properties of this sample.

References

1. Diouf B, Pode R (2015) Potential of lithium-ion batteries in renewable energy. Renew Energy 76:375–380. https://doi.org/10.1016/j.renene.2014.11.058

2. Bakenov Z, Taniguchi I (2010) Physical and electrochemical properties of LiMnPO$_4$/C composite cathode prepared with different conductive carbons. J Power Sources 195:7445–7451. https://doi.org/10.1016/j.jpowsour.2010.05.023

3. Konarova M, Taniguchi I (2010) Synthesis of carbon-coated LiFePO$_4$ nanoparticles with high rate performance in lithium secondary batteries. J Power Sources 195:3661–3667. https://doi.org/10.1016/j.jpowsour.2009.11.147

4. Bakenov Z, Taniguchi I (2010) Electrochemical performance of nanocomposite LiMnPO$_4$/C cathode materials for lithium batteries. Electrochem Commun 12:75–78. https://doi.org/10.1016/j.elecom.2009.10.039

5. Asenbauer J, Eisenmann T, Kuenzel M, Kazzazi A, Chen Z, Bresser D (2020) The success story of graphite as a lithium-ion anode material – fundamentals, remaining challenges, and recent developments including silicon (oxide) composites. Sustain Energy Fuels 4:5387–5416. https://doi.org/10.1039/d0se00175a

6. Kim DS, Chung DJ, Bae J, Jeong G, Kim H (2017) Surface engineering of graphite anode material with black TiO$_{2-x}$ for fast chargeable lithium ion battery. Electrochim Acta 258:336–342. https://doi.org/10.1016/j.electacta.2017.11.056

7. Mitra S, Poizot P, Finke A, Tarascon JM (2006) Growth and electrochemical characterization versus lithium of Fe$_3$O$_4$ electrodes made via electrodeposition. Adv Funct Mater 16:2281–2287. https://doi.org/10.1002/adfm.200500753

8. Taberna PL, Mitra S, Poizot P, Simon P, Tarascon JM (2006) High rate capabilities Fe$_3$O$_4$-based Cu nano-architectured electrodes for lithium-ion battery applications. Nat Mater 5:567–573. https://doi.org/10.1038/nmat1672

9. Muraliganth T, Vadivel Murugan A, Manthiram A (2009) Facile synthesis of carbon-decorated single-crystalline Fe$_3$O$_4$ nanowires and their application as high performance anode in lithium ion batteries. Chem Commun 7360–7362. https://doi.org/10.1039/b916376j

10. He Y, Huang L, Cai JS, Zheng XM, Sun SG (2010) Structure and electrochemical performance of nanostructured Fe$_3$O$_4$/carbon nanotube composites as anodes for lithium ion batteries. Electrochim Acta 55:1140–1144. https://doi.org/10.1016/j.electacta.2009.10.014

11. Li L, Kovalchuk A, Fei H, Peng Z, Li Y, Kim ND, Xiang C, Yang Y, Ruan G, Tour JM (2015) Enhanced cycling stability of lithium-ion batteries using graphene-wrapped Fe$_3$O$_4$-graphene nanoribbons as anode materials. Adv Energy Mater 5:1500171–1500176. https://doi.org/10.1002/aenm.201500171

12. Liu Z, Yu XY, Paik U (2016) Etching-in-a-box: A novel strategy to synthesize unique yolk-shelled Fe$_3$O$_4$@carbon with an ultralong cycling life for lithium storage. Adv Energy Mater 6:3–7. https://doi.org/10.1002/aenm.201502318

13. Behera SK (2011) Facile synthesis and electrochemical properties of Fe$_3$O$_4$ nanoparticles for Li ion battery anode. J Power Sources 196:8669–8674. https://doi.org/10.1016/j.jpowsour.2011.06.067

14. Belgibayeva A, Taniguchi I (2019) Synthesis and characterization of SiO$_2$/C composite nanofibers as free-standing anode materials for Li-ion batteries. Electrochim Acta 328:135101–135122. https://doi.org/10.1016/j.electacta.2019.135101

15. Zhang Y, Li Y, Li H, Zhao Y, Yin F, Bakenov Z (2016) Electrochemical performance of carbon-encapsulated Fe$_3$O$_4$ nanoparticles in lithium-ion batteries: morphology and particle size effects. Electrochim Acta 216:475–483. https://doi.org/10.1016/j.electacta.2016.09.054

16. Guo C, Wang L, Zhu Y, Wang D, Yang Q, Qian Y (2015) Fe$_3$O$_4$ nanoflakes in an N-doped carbon matrix as high-performance anodes for lithium ion batteries. Nanoscale 7:10123–10129. https://doi.org/10.1039/c5nr01953b

17. Zhao N, Wu S, He C, Wang Z, Shi C, Liu E, Li J (2013) One-pot synthesis of uniform Fe$_3$O$_4$ nanocrystals encapsulated in interconnected carbon nanospheres for superior lithium storage capability. Carbon N Y 57:130–138. https://doi.org/10.1016/J.CARBON.2013.01.056

18. Behera SK (2011) Enhanced rate performance and cyclic stability of Fe$_3$O$_4$-graphene nanocomposites for Li ion battery anodes. Chem Commun 47:10371–10373. https://doi.org/10.1039/c1cc13218k

19. Lu G, Qiu S, Liu J, Wang X, He C, Bai YJ (2014) Enhanced electrochemical performance of Zn-doped Fe$_3$O$_4$ with carbon coating. Electrochim Acta 117:230–238. https://doi.org/10.1016/j.electacta.2013.11.133

20. Wang L, Yu Y, Chen PC, Zhang DW, Chen CH (2008) Electrospinning synthesis of C/Fe$_3$O$_4$ composite nanofibers and their application for high performance lithium-ion batteries. J Power Sources 183:717–723. https://doi.org/10.1016/j.jpowsour.2008.05.079

21. Guo L, Sun H, Qin C, Li W, Wang F, Song W, Du J, Zhong F, Ding Y (2018) Flexible Fe$_3$O$_4$ nanoparticles/N-doped carbon nanofibers hybrid film as binder-free anode materials for lithium-ion batteries. Appl Surf Sci 459:263–270. https://doi.org/10.1016/j.apsusc.2018.08.001

22. Patil PS (1999) Versatility of chemical spray pyrolysis technique. Mater Chem Phys 59:185–198. https://doi.org/10.1016/S0254-0584(99)00049-8

23. Suh WH, Suslick KS (2005) Magnetic and porous nanospheres from ultrasonic spray pyrolysis. J Am Chem Soc 127:12007–12010. https://doi.org/10.1021/ja050693p

24. Taniguchi I, Lim CK, Song D, Wakihara M (2022) Particle morphology and electrochemical performances of spinel LiMn$_2$O$_4$ powders synthesized using ultrasonic spray pyrolysis method. Solid State Ionics 146:239–247. https://doi.org/10.1016/S0167-2738(01)01016-5

25. Deng W, Ci S, Li H, Wen Z (2017) One-step ultrasonic spray route for rapid preparation of hollow Fe$_3$O$_4$/C microspheres anode for lithium-ion batteries. Chem Eng J 330:995–1001. https://doi.org/10.1016/j.cej.2017.08.039

26. Choi SH, Ko YN, Jung KY, Kang YC (2014) Macroporous Fe$_3$O$_4$/carbon composite microspheres with a short Li$^+$ diffusion pathway for the fast charge/discharge of lithium ion batteries. Chem-A Eur J 20:11078–11083. https://doi.org/10.1002/chem.201402359

27. Atkinson JD, Fortunato ME, Dastgheib SA, Rostam-Abadi M, Rood MJ, Suslick KS (2011) Synthesis and characterization of iron-impregnated porous carbon spheres prepared by ultrasonic spray pyrolysis. Carbon N Y 49:587–598. https://doi.org/10.1016/j.carbon.2010.10.001

28. Adi A, Taniguchi I (2022) Synthesis and characterization of porous-crystalline C/Fe$_3$O$_4$ microspheres by spray pyrolysis with steam oxidation as anode materials for Li-ion batteries. Adv Powder Technol 33:103606–103616. https://doi.org/10.1016/J.APT.2022.103606

29. Taniguchi I, Fukuda N, Konarova M (2008) Synthesis of spherical LiMn$_2$O$_4$ microparticles by a combination of spray pyrolysis and drying method. Powder Technol 181:228–236. https://doi.org/10.1016/j.powtec.2007.05.011

30. Xu C, Niu D, Zheng N, Yu H, He J, Li Y (2018) Facile synthesis of nitrogen-doped double-shelled hollow mesoporous carbon nanospheres as high-performance anode materials for lithium ion batteries. ACS Sustain Chem Eng 6:5999–6007. https://doi.org/10.1021/acssuschemeng.7b04617

31. Su D, Ahn HJ, Wang G (2013) One-dimensional magnetite Fe$_3$O$_4$ nanowires as electrode material for Li-ion batteries with improved electrochemical performance. J Power Sources 244:742–746. https://doi.org/10.1016/j.jpowsour.2012.11.058

32. Gao G, Lu S, Dong B, Zhang Z, Zheng Y, Ding S (2015) One-pot synthesis of carbon coated Fe$_3$O$_4$ nanosheets with superior lithium storage capability. J Mater Chem A 3:4716–4721. https://doi.org/10.1039/c4ta05725b

33. Sun X, Zheng C, Zhang F, Yang Y, Wu G, Yu A, Guan N (2009) Size-controlled synthesis of magnetite (Fe$_3$O$_4$) nanoparticles coated with glucose and gluconic acid from a single Fe(III) precursor by a sucrose bifunctional hydrothermal method. J Phys Chem C 113(2009):16002–16008. https://doi.org/10.1021/jp9038682

34. Eslamian M, Ahmed M, Ashgriz N (2006) Modelling of nanoparticle formation during spray pyrolysis Related content Modelling of nanoparticle formation during spray pyrolysis. Nanotechnology 17:1674–1685. https://doi.org/10.1088/0957-4484/17/6/023

35. Leng J, Wang Z, Wang J, Wu HH, Yan G, Li X, Guo H, Liu Y, Zhang Q, Guo Z (2019) Advances in nanostructures fabricated: Via spray pyrolysis and their applications in energy storage and conversion. Chem Soc Rev 48:3015–3072. https://doi.org/10.1039/c8cs00904j

36. Sing KSW, Everett DH, Haul RAW, Moscou L, Pierotti RA, Rouquerol J, Siemieniewska T (1985) Reporting physisorption data for gas/solid systems with special reference to the determination of surface area and porosity. Pure Appl Chem 57:603–619. https://doi.org/10.1351/pac198557040603

37. Ferrari AC, Robertson J (2000) Interpretation of Raman spectra of disordered and amorphous carbon. Phys Rev B 61:14095–14107

38. Tunistra F, Koenig JL (1970) Raman spectrum of graphite. J Chem Phys 53:1126–1130. https://doi.org/10.1063/1.1674108

39. Wang Y, Gao Y, Shao J, Holze R, Chen Z, Yun Y, Qu Q, Zheng H (2018) Ultrasmall Fe$_3$O$_4$ nanodots within N-doped carbon frameworks from MOFs uniformly anchored on carbon nanowebs for boosting Li-ion storage. J Mater Chem A 6:3659–3666. https://doi.org/10.1039/c7ta10330a

40. Seredych M, Hulicova-Jurcakova D, Lu GQ, Bandosz TJ (2008) Surface functional groups of carbons and the effects of their chemical character, density and accessibility to ions on electrochemical performance. Carbon N Y 46:1475–1488. https://doi.org/10.1016/j.carbon.2008.06.027

41. Richards GN, Shafizadeh F (1978) Mechanism of thermal degradation of sucrose. a preliminary study. Aust J Chem 31:1825–1832. https://doi.org/10.1071/CH9781825

42. Ma FX, Bin WuH, Xu CY, Zhen L, Lou XW (2015) Self-organized sheaf-like Fe$_3$O$_4$/C hierarchical microrods with superior lithium storage properties. Nanoscale 7:4411–4414. https://doi.org/10.1039/c5nr00046g

43. Piao Y, Kim HS, Sung YE, Hyeon T (2010) Facile scalable synthesis of magnetite nanocrystals embedded in carbon matrix as superior anode materials for lithium-ion batteries. Chem Commun 46:118–120. https://doi.org/10.1039/b920037a

44. Kwon TG, Park H, Jo OH, Chun J, Kang BG (2022) Facile preparation of magnetite-incorporated polyacrylonitrile-derived carbons for Li-ion battery anodes. ACS Appl Energy Mater 5:1262–1270. https://doi.org/10.1021/ACSAEM.1C03679/ASSET/IMAGES/LARGE/AE1C03679_0008.JPEG

45. Wang JZ, Zhong C, Wexler D, Idris NH, Wang ZX, Chen LQ, Liu HK (2011) Graphene-encapsulated Fe$_3$O$_4$ nanoparticles with 3D laminated structure as superior anode in lithium ion batteries. Chem A Eur J 17:661–667. https://doi.org/10.1002/CHEM.201001348

46. Venkatachalam S, Zhu H, Masarapu C, Hung KH, Liu Z, Suenaga K, Wei B (2009) In-situ formation of sandwiched structures of nanotube/Cu$_x$O$_y$/Cu composites for lithium battery applications. ACS Nano 3:2177–2184. https://doi.org/10.1021/NN900432U/SUPPL_FILE/NN900432U_SI_001.PDF

47. Mao Y, Duan H, Xu B, Zhang L, Hu Y, Zhao C, Wang Z, Chen L, Yang Y (2012) Lithium storage in nitrogen-rich mesoporous carbon materials. Energy Environ Sci 5:7950–7955. https://doi.org/10.1039/c2ee21817h